Chapter 2
Monolayer Graphene on a hBN Underlay

2.1 Introduction

It has been demonstrated that the electronic quality of graphene-based devices can be dramatically improved by placing graphene on an atomically flat crystal surface, such as hexagonal boron nitride (hBN) [1–7]. At the same time, graphene's electronic spectrum also becomes modified, acquiring a complex, energy-dependent form caused by incommensurability between the graphene and substrate crystal lattices [8–11]. For graphene placed on hBN, the moire pattern [2, 4, 8–11] creates a periodic perturbation, usually referred to as a superlattice, which acts on graphene's charge carriers and leads to multiple minibands [12] and the generation of secondary Dirac-like spectra. The resulting new Dirac fermions present yet another case where graphene allows mimicking of QED phenomena under conditions that cannot be achieved in particle physics experiments. In contrast to relativistic particles in free space, the properties of secondary Dirac fermions in graphene can be affected by a periodic sublattice symmetry breaking and modulation of carbon-carbon hopping amplitudes, in addition to a simple potential modulation. The combination of different features in the modulation results in a multiplicity of possible outcomes for the moiré miniband spectrum in graphene which we systematically investigate in this chapter.

2.2 Superlattice Hamiltonian

To describe the effect of a substrate on electrons in graphene at a distance, d, much larger than graphene's lattice constant, a, we use the earlier observation [8–10, 13–16] that, at $d \gg a$, the lateral variation of the wavefunctions of the $2p_z$ carbon orbitals is smooth on the scale of a. This is manifested in the comparable sizes of the skew and vertical hopping in graphite and permits an elegant continuum-model description [13–16] of the interlayer coupling in twisted bilayers

J. R. Wallbank, *Electronic Properties of Graphene Heterostructures with Hexagonal Crystals*, Springer Theses, DOI: 10.1007/978-3-319-07722-2_2,

and the resulting band structure. A similar idea applied to graphene on a hBN substrate [8–10] suggests that a substrate perturbation for Dirac electrons in graphene can be described in terms of simple harmonic functions corresponding to the six smallest reciprocal lattice vectors of the moiré superlattice.

Below, we shall use a similar approach to analyse the generic properties of moiré minibands for electrons in graphene subjected to a substrate with a hexagonal Bravais lattice with a slightly different lattice constant of $(1+\delta)a$, $|\delta| \ll 1$, compared to that of a for graphene, and a small misalignment angle, $\theta \ll 1$. The moiré pattern harmonics are described by vectors

$$\boldsymbol{b}_{m=0,\ldots 5} = \hat{R}_{\frac{2\pi m}{6}} \boldsymbol{b}_0, \quad \boldsymbol{b}_0 = \left[1-(1+\delta)^{-1}\hat{R}_\theta\right]\left(0, \frac{4\pi}{\sqrt{3}a}\right), \tag{2.1}$$

with length $|\boldsymbol{b}_0| \equiv b \approx \frac{4\pi}{\sqrt{3}a}\sqrt{\delta^2+\theta^2}$, which can be obtained from each other by the anticlockwise rotation, $\hat{R}_{2\pi m/6}$. For a substrate with a simple hexagonal lattice or a honeycomb lattice with two identical atoms, the perturbation created for graphene electrons is inversion-symmetric. For a honeycomb substrate where one of the atoms would affect graphene electrons stronger than the other (e.g. such as hBN, for which the occupancy and size of the $2p_z$ orbitals are different) the moiré potential can be modelled as a combination of a dominant inversion-symmetric part with the addition of a small inversion-asymmetric perturbation,

$$\begin{aligned}\hat{H} = {} & v\boldsymbol{p}\cdot\boldsymbol{\sigma} + u_0 vbf_1(\boldsymbol{r}) + u_3 vbf_2(\boldsymbol{r})\sigma_3\tau_3 + u_1 v\left[\boldsymbol{l}_z\times\nabla f_2(\boldsymbol{r})\right]\cdot\boldsymbol{\sigma}\tau_3 + u_2 v\nabla f_2(\boldsymbol{r})\cdot\boldsymbol{\sigma}\tau_3 \\ & + \tilde{u}_0 vbf_2(\boldsymbol{r}) + \tilde{u}_3 vbf_1(\boldsymbol{r})\sigma_3\tau_3 + \tilde{u}_1 v\left[\boldsymbol{l}_z\times\nabla f_1(\boldsymbol{r})\right]\cdot\boldsymbol{\sigma}\tau_3 + \tilde{u}_2 v\nabla f_1(\boldsymbol{r})\cdot\boldsymbol{\sigma}\tau_3.\end{aligned} \tag{2.2}$$

The Hamiltonian, $\hat{H}$, is written in terms of direct products $\sigma_i\tau_j$, of the Pauli matrices described in Sect. 1.5.2. The first term in $\hat{H}$ is the Dirac part, with $\boldsymbol{p} = -i\nabla + e\boldsymbol{A}$ describing the momentum relative to the centre of the corresponding valley, with $\nabla\times\boldsymbol{A} = B$. The rest of the first line in Eq. (2.2) describes the inversion-symmetric part of the moiré perturbation, whereas the second line takes into account its inversion-asymmetric part. In the first line, the first term, with $f_1(\boldsymbol{r}) = \sum_{m=0\ldots5} e^{i\boldsymbol{b}_m\cdot\boldsymbol{r}}$, describes a simple potential modulation. The second term, with $f_2(\boldsymbol{r}) = i\sum_{m=0\ldots5}(-1)^m e^{i\boldsymbol{b}_m\cdot\boldsymbol{r}}$, accounts for the A–B sublattice asymmetry, locally imposed by the substrate. The third term, with unit vector $\boldsymbol{l}_z$, describes the influence of the substrate on the A–B hopping: consequently [17–19], this term can be associated with a pseudo-magnetic field, $eB^{\text{eff}} = \pm u_1 b^2 f_2(\boldsymbol{r})$, which has opposite signs in valleys $K_\pm$. Each of the coefficients $|u_i| \ll 1$ in Eq. (2.2) is a dimensionless phenomenological parameter with the energy scale set by $vb \approx 2\pi\sqrt{\delta^2+\theta^2}\gamma_0$, where $\gamma_0 \approx 3$ eV is the nearest neighbour hopping integral in the Slonczewski-Weiss tight binding model [20]. Concerning the inversion-asymmetric part, the second line in Eq. (2.2), we assume that $|\tilde{u}_i| \ll |u_i|$. Note that the last term in each line can be gauged away using $\psi \to e^{-i\tau_3(u_2 f_2 + \tilde{u}_2 f_1)}\psi$.

Table 2.1 The inversion-symmetric parameters, vbu_i, for various models of the moiré superlattice

Model	vbu_0 [meV]	vbu_1 [meV]	vbu_2 [meV]	vbu_3 [meV]
Potential modulation [8]	60	0	0	0
2D charge modulation [9]	$-\frac{V_0}{2}$	0	0	$\frac{\sqrt{3}V_0}{2}$
One-site version of G-hBN hopping [10] (Sect. 2.6.2)	1.6	$\frac{-3.2\delta}{\sqrt{\delta^2+\theta^2}}$	$\frac{3.2\theta}{\sqrt{\delta^2+\theta^2}}$	-2.8
Point charge lattice (Sect. 2.6.1), $0.6 \le \tilde{v} \le 3.4$	$\frac{\tilde{v}}{2}$	$\frac{-\tilde{v}\delta}{\sqrt{\delta^2+\theta^2}}$	$\frac{\tilde{v}\theta}{\sqrt{\delta^2+\theta^2}}$	$-\frac{\sqrt{3}\tilde{v}}{2}$

In the 2D charge modulation model [9], V_0 is a phenomenological parameter. The G-hBN hopping model in Ref. [10] used the hopping parameter from twisted bilayer graphene. Estimates in Sects. 2.6.1 and 2.6.2 show that the sets of parameters using a model of point charges attributed to nitrogen sites and for the G-hBN hopping model are very similar

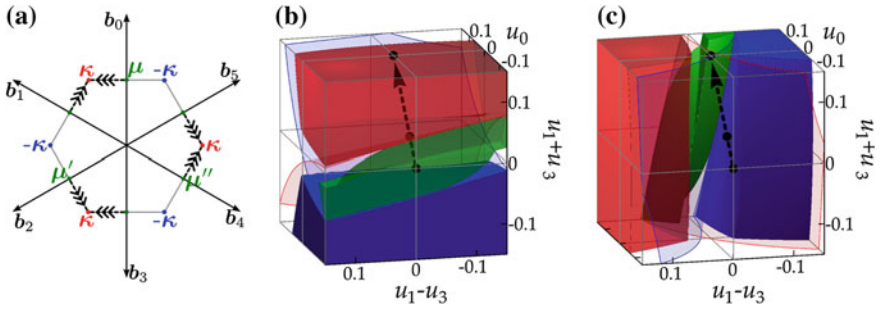

Fig. 2.1 **a** The hexagonal Brillouin zone for the moiré superlattice. **b** Three volumes in the space of the moiré superlattice parameters where the edge of the first miniband, in graphene's valence band, contains an isolated sDP at the $\boldsymbol{\kappa}$-point (*red*) or the $-\boldsymbol{\kappa}$-point (*blue*) or three isolated sDPs at the sBZ edge (*green*). Parameters for which the $\pm\boldsymbol{\kappa}$-point is triple degenerate are shown by the *red* and *blue* surfaces. The *black dots* represent sets of perturbation parameters for which miniband spectra are shown in Fig. 2.2. **c** The same for the conduction band in graphene

Hamiltonian, $\hat{H}$, may be used to parametrise any microscopic model compatible with the symmetries of the system (see Sect. 2.5) and the dominance of the simplest moiré harmonics, $e^{i\boldsymbol{b}_m\cdot\boldsymbol{r}}$, in the superlattice perturbation. The values that parameters u_i take are listed in Table 2.1 for several models of graphene on an hBN substrate, both taken from the recent literature [8–10] and analysed in Sects. 2.6.1 and 2.6.2, including a simple model in which the hBN substrate is treated as a lattice of positively charged nitrogen nuclei with a compensating homogeneous background of electron $2p_z$ orbitals. The examples of model-dependent values of parameters u_i, listed in Table 2.1, indicate that the combination of several factors can strongly shift the resulting moiré perturbation across the parameter space in Fig. 2.1. That is why, in this chapter, we analyse the generic features of the miniband spectra generated by the moiré superlattice, rather than attempt to make a brave prediction about its exact form for a particular substrate.

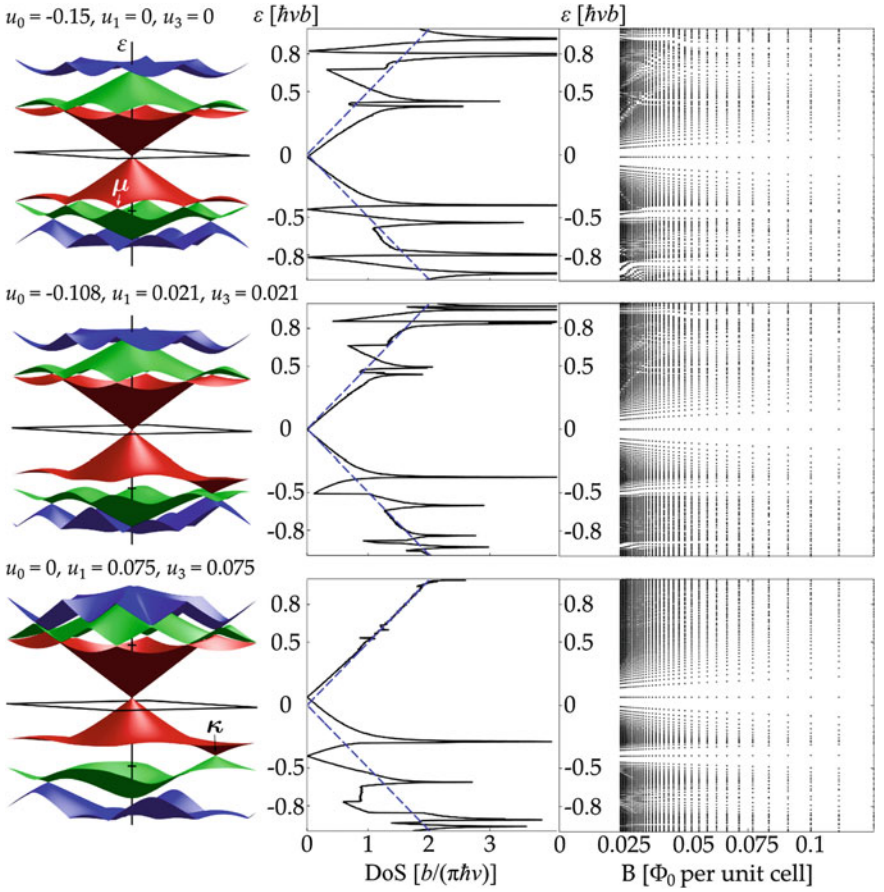

Fig. 2.2 Numerically calculated moiré miniband (*left*), the corresponding density of states (*centre*), and Landau level spectrum (*right*) for electrons in the vicinity of graphene's K point. Here we use the rhombic sBZ, so that the c_{3v} symmetry of the moiré superlattice spectrum is not obviously seen in the images

In the absence of a magnetic field, the Hamiltonian Eq. (2.2) obeys time-reversal symmetry, which follows from both σ_i and τ_i changing sign upon the transformation $t \to -t$ (Sect. 1.5.4). As a result, $\epsilon_{\boldsymbol{K}_+ + \boldsymbol{p}} = \epsilon_{\boldsymbol{K}_- - \boldsymbol{p}}$ and we limit the discussion of minibands to the K_+ valley. Subject to this limitation, the bandstructure for the inversion-symmetric superlattice perturbation obeys the c_{3v} symmetry. Moreover, using the commutation properties of σ_i one can establish that

$$\epsilon^{u_0,u_1,u_3}_{\boldsymbol{K}_+ + \boldsymbol{p}} = -\epsilon^{-u_0,-u_1,u_3}_{\boldsymbol{K}_+ - \boldsymbol{p}} = -\epsilon^{-u_0,u_1,-u_3}_{\boldsymbol{K}_+ + \boldsymbol{p}} = \epsilon^{u_0,-u_1,-u_3}_{\boldsymbol{K}_+ - \boldsymbol{p}}. \tag{2.3}$$

2.3 Generic Miniband Spectra of Graphene-hBN Heterostructures

To calculate the miniband spectrum for $\hat{H}$ in Eq. (2.2) we perform zone folding (in the graphene K_+ valley) bringing states with momenta related by the reciprocal lattice vectors $n_1\boldsymbol{b}_1 + n_2\boldsymbol{b}_2$ of the moiré pattern to the same point of the superlattice Brillouin zone (sBZ) in Fig. 2.1a. Then, we calculate the matrix elements of $\hat{H}$ between those states and diagonalise the corresponding Heisenberg matrix numerically exploring the parametric space (u_0, u_1, u_3) of the dominant inversion-symmetric part of the moiré perturbation shown in Fig. 2.1b, c. The size of the matrix is chosen to guarantee the convergence of the calculated energies for the three lowest minibands in both the conduction band ($s = +1$) and the valence band ($s = -1$). Below, we discuss the generic features of the moiré miniband spectra for the characteristic points in the parametric space (u_0, u_1, u_3), marked using black dots in Fig. 2.1b, c, using both the numerically calculated dispersion surfaces in Fig. 2.2 and analytical perturbation theory analysis.

For the zero-energy Dirac point in graphene, there are only the original $\boldsymbol{p} = 0$ states in each valley that appear at $\epsilon = 0$ upon zone folding. For all three characteristic spectra shown in Fig. 2.2, for the inversion-symmetric moiré perturbation, the gapless Dirac spectrum persists at low energies near the conduction-valence band edge with almost unchanged Dirac velocity, $\left[1 + O(u^2)\right] v$. The inversion-asymmetric terms $\tilde{u}_i$ are able [10] to open a minigap at the Dirac point,

$$\Delta_0 = 24vb|u_1\tilde{u}_0 + u_0\tilde{u}_1|. \tag{2.4}$$

For the point $\boldsymbol{\mu} = \boldsymbol{b}_0/2$ on the edge of the first sBZ, zone folding brings together two degenerate plane wave states, $|\boldsymbol{\mu} + \boldsymbol{q}\rangle$ and $|\boldsymbol{\mu} + \boldsymbol{b}_3 + \boldsymbol{q}\rangle$. The splitting of these degenerate states by the moiré potential in Eq. (2.2) can be studied using degenerate perturbation theory. The corresponding 2×2 matrix, expanded in small deviation $\boldsymbol{q}$ of the electron momentum from each of the three sBZ $\boldsymbol{\mu}$-points[1] has the form

$$\begin{aligned}
\hat{H}_{\boldsymbol{\mu}+\boldsymbol{q}} &= vb\begin{pmatrix} E_{\boldsymbol{\mu}} + s\frac{q_y}{b} & H_{12} \\ H_{12}^* & E_{\boldsymbol{\mu}} - s\frac{q_y}{b} \end{pmatrix}, \\
E_{\boldsymbol{\mu}} &\approx \frac{s}{2} + \frac{sq_x^2}{b^2}, \\
H_{12} &\approx (su_1 - u_3) - i(s\tilde{u}_1 - \tilde{u}_3) + 2\frac{q_x}{b}(u_0 + i\tilde{u}_0).
\end{aligned} \tag{2.5}$$

For the inversion-symmetric perturbation, the dispersion relation resulting from Eq. (2.5) contains an anisotropic secondary Dirac point (sDP) [8, 21, 22] with Dirac

[1] The Hamiltonian in the vicinity of other two inequivalent points on the sBZ edge, $\boldsymbol{\mu}' = \hat{R}_{2\pi/3}\boldsymbol{\mu}$, $\boldsymbol{\mu}'' = \hat{R}_{4\pi/3}\boldsymbol{\mu}$, can be obtained using $H_{\boldsymbol{\mu}+\boldsymbol{q}} = H_{\boldsymbol{\mu}'+\hat{R}_{2\pi/3}\boldsymbol{q}} = H_{\boldsymbol{\mu}''+\hat{R}_{4\pi/3}\boldsymbol{q}}$.

velocity component $\approx 2u_0 v$ in the direction of the sBZ edge and $\approx v$ in the perpendicular direction. This feature is clearly seen at the $\boldsymbol{\mu}$-point of the first moiré miniband in the valence band, in the top row of Fig. 2.2. Note that the electron spectrum is not symmetric between the valence and conduction bands and that the sDPs at the $\boldsymbol{\mu}$-point in the conduction band are obscured by an overlapping spectral branch.

Moving in parameter space, e.g., along the line shown in Fig. 2.1b, the positions of the three anisotropic sDPs shift along the sBZ edge towards the sBZ corners: either $\boldsymbol{\kappa} = (\boldsymbol{b}_4 + \boldsymbol{b}_5)/3$, or $-\boldsymbol{\kappa}$, as shown by arrowed lines in Fig. 2.1a. In general, a spectrum with three isolated sDPs at the sBZ edge is typical for the green volume in the parameter space in Fig. 2.1b for the valence band, or Fig. 2.1c for the conduction band. In contrast, for (u_0, u_1, u_3) in the clear part of the parameter space, sDPs on the edge of the first sBZ are overshadowed by an overlapping spectral branch, as is the case on the conduction band side for all three cases shown in Fig. 2.2.

For the points in Fig. 2.1b, c on the red and blue surfaces, the three sDPs reach the $\boldsymbol{\kappa}$-point, forming a triple degenerate band crossing, as in the valence band spectrum shown in the middle row of Fig. 2.2, which can be traced using the perturbation theory analysis of the band crossing at $\boldsymbol{\kappa}$ discussed below.

The third line in Fig. 2.2 shows the third type of spectrum of moiré minibands, characteristic for the red and blue volumes of the parameter space in Fig. 2.1. The characteristic feature of such spectra consist of a single isolated sDP, at the $\pm\boldsymbol{\kappa}$-point, in the valence band (Fig. 2.1b) or the conduction band (Fig. 2.1c).

For the $\boldsymbol{\kappa}$ and $-\boldsymbol{\kappa}$-points, zone folding brings together three degenerate plane wave states, $|\zeta(\boldsymbol{\kappa}+\boldsymbol{q})\rangle$, $|\zeta(\boldsymbol{\kappa}+\boldsymbol{b}_1+\boldsymbol{q})\rangle$, and $|\zeta(\boldsymbol{\kappa}+\boldsymbol{b}_2+\boldsymbol{q})\rangle$ (where $\zeta = \pm$), whose splitting is determined by

$$\hat{H}_{\zeta(\boldsymbol{\kappa}+\boldsymbol{q})} = vb \begin{pmatrix} \frac{s}{\sqrt{3}} + \frac{sq_x}{b} & w_\zeta & w_\zeta^* \\ w_\zeta^* & \frac{s}{\sqrt{3}} - s\frac{q_x - \sqrt{3}q_y}{2b} & -w_\zeta \\ w_\zeta & -w_\zeta^* & \frac{s}{\sqrt{3}} - s\frac{q_x + \sqrt{3}q_y}{2b} \end{pmatrix},$$

$$w_\zeta \approx \frac{1}{2}\Big[\Big(u_0 - 2s\zeta u_1 + \sqrt{3}\zeta u_3\Big) + i\zeta\Big(\tilde{u}_0 + 2s\zeta\tilde{u}_1 - \sqrt{3}\zeta\tilde{u}_3\Big)\Big]. \tag{2.6}$$

For $w_\zeta \neq 0$, the inversion-symmetric terms in $\hat{H}_{\zeta(\boldsymbol{\kappa}+\boldsymbol{q})}$ partially lift the $\zeta\boldsymbol{\kappa}$-point degeneracy into a singlet with energy $(\frac{s}{\sqrt{3}} - 2w_\zeta)vb$ and a doublet with energies $(\frac{s}{\sqrt{3}} + w_\zeta)vb$, so that a distinctive sDP [22] characterised by Dirac velocity $v_{\boldsymbol{\kappa}} = [1 + O(u)]\,\frac{v}{2}$ [9] is always present at $\pm\boldsymbol{\kappa}$ somewhere in the spectrum.[2] This behaviour reflects the generic properties of the symmetry group of wave vector $\boldsymbol{\kappa}$, detailed in Sect. 2.5, which has the two-dimensional irreducible representation E (corresponding to the sDP) and one-dimensional irreducible representations A_1 and A_2. Note that each isolated sDP is surrounded by Van Hove singularities in the density of states corresponding to saddle points in the lowest energy minibands. The weaker inversion-asymmetric terms, $|\tilde{u}_i| \ll |u_i|$, in the second line of Eq. (2.2), open

[2] Note that the spectra derived from $\hat{H}_{\zeta(\boldsymbol{\kappa}+\boldsymbol{q})}$ obey the three-fold rotational symmetry.

a minigap in both types of sDP discussed above. The perturbation theory leading to Eq. (2.5) and Eq. (2.6) has been performed to greater accuracy, and the sDP positions have been tracked in greater detail, in Appendix A.

The appearance of sDPs at the edge of the first miniband results in a peculiar spectrum of electronic Landau levels, as shown on the r.h.s of Fig. 2.2. Each data point in these spectra represents one of the Hofstadter minibands [23] (with an indistinguishably small width) calculated for rational values of magnetic flux, $\frac{p}{q}\Phi_0$ per moiré supercell following a method in Ref. [15]. Using these spectra one can trace a clearly separated "zero-energy" Landau level related to the isolated $\boldsymbol{\kappa}$-point sDP in the valence band in the bottom row of Fig. 2.2, in addition to the true zero-energy Landau level at the conduction-valence band edge. The three isolated sDPs on the sBZ edge in the valence band (top row of Fig. 2.2) also result in a "zero-energy" Landau level, though not as clearly separated and split by the magnetic breakdown occurring at $\Phi \approx 0.1\Phi_0$.

2.4 Effect of the Miniband Spectra on the Hall Coefficient

The inversion-symmetric moiré perturbation will result in either the first sBZ separated from the rest of the spectrum by one or three sDPs, or, for weak perturbations, will result in overlapping first and higher minibands. The experimental consequences of this consists in a non-monotonic variation of the Hall coefficient upon doping the graphene flake with electrons or holes. For example, for those miniband spectra in Fig. 2.2, where there are isolated sDPs in the valence band, the Hall coefficient would pass through a zero value and change sign at two characteristic densities, n_1 and n_2. At the density n_1, which corresponds to the valence band filled with holes up to the Van Hove singularity, the Hall coefficient will change sign from positive to negative. At the higher density, n_2, which corresponds to a completely filled first miniband, it would repeat the behaviour at the neutrality point changing sign from negative to positive. Such behaviour is expected to take place for the entire regions of the parametric space painted red, blue or green in Fig. 2.1. The relation between these two carrier densities for various types and strengths of moiré perturbations is shown in Fig. 2.3. This behaviour was observed in experimental results discussed in Chap. 5. For the clear part of the parametric space for which we find substantial overlap between many moiré minibands such alternations in the sign of the Hall coefficient would be obscured by the competing contributions from the "electron-like" and "hole-like" branches in the spectrum.

2.5 Symmetry of the Moiré Superlattice

We now discuss the consequences of the moiré superlattice symmetry, both for Hamiltonian (2.2) and the sDP. The point group symmetry of graphene on an incommensurate substrate is given by the intersection of the point group of graphene, c_{6v}, with

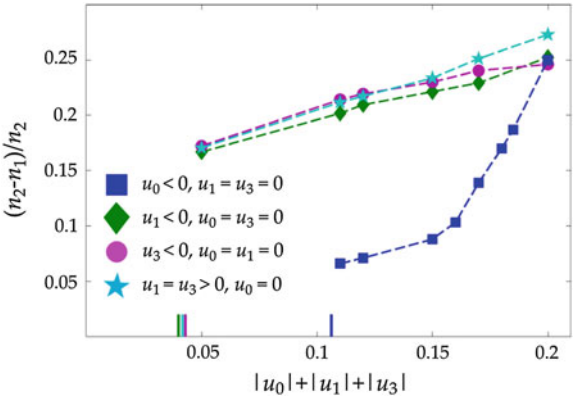

Fig. 2.3 The relation between the two densities at which the Hall coefficient in graphene reverses sign upon its doping with holes. The results are shown for several realisations of moiré superlattice in the parameter range corresponding to either three isolated sDPs on the sBZ edge (*squares*) or one isolated sDP at the sBZ corner (*other symbols*). The thresholds for isolation are indicated on the x-axis

that of its substrate. For a perfectly aligned ($\theta = 0$) inversion-symmetric substrate, with either a single (dominant) atom per unit cell or two identical atoms arranged in a honeycomb lattice, the point group symmetries of the substrate and graphene coincide. The corresponding Hamiltonian, Eq. (2.2), with moiré harmonics orientated as per Fig. 2.1a, must necessarily commute with the operators corresponding to the elements of c_{6v}: $\hat{c}_6$, $\hat{s}_x$ and $\hat{s}_y$ which describe $2\pi/6$ rotations and reflections that either exchange or preserve the graphene sublattices. The operators for $\hat{c}_6$ and $\hat{s}_y$ involve the valley exchanging matrices $\tau_{1,2}$ with the result that the symmetry of the Hamiltonian restricted to the K valley, as well as the K valley bandstructure, is reduced to $c_{3v} = \{id, \hat{c}_3, \hat{s}_x\}$, where $\hat{c}_3 = \hat{c}_6^2$ has no intervalley structure. Each of the $\tilde{u}_i$ terms are odd under $\hat{c}_6$, while the u_2 and $\tilde{u}_2$ terms are odd under $\hat{s}_y$, so that these terms are forbidden for the perfectly aligned inversion-symmetric system described above. The point group of substrates with the honeycomb lattice and two non-equivalent atoms per unit cell, such as hBN, only possesses the $\hat{c}_3$ and $\hat{s}_y$ symmetries which allow inversion-asymmetric parameters $\tilde{u}_{i=0,1,3}$ to take a finite value.

For a finite misalignment angle, the reflection symmetries of graphene and the substrate do not coincide, and the moiré harmonics become misaligned, by an angle ϕ, from those in Fig. 2.1a. However, the moiré harmonics may be brought back into alignment using the transformation $\hat{H}(\boldsymbol{r}) \rightarrow e^{i\sigma_3 \frac{\phi}{2}} \hat{H}(\hat{R}_\phi \boldsymbol{r}) e^{-i\sigma_3 \frac{\phi}{2}}$, and the u_2 and $\tilde{u}_2$ terms, which are no longer forbidden, may be gauged away. This procedure restores the reflection symmetries to the Hamiltonian, despite their absence in the geometry of the moiré pattern for finite misalignment angle.

The symmetries described above can be used to gain a deeper understanding of the sDPs discussed in the main text. The K valley plane wave states from the three equivalent sBZ corners, $\zeta\boldsymbol{\kappa}_{n=0,1,2} = \zeta \hat{R}_{2\pi n/3}\boldsymbol{\kappa}$, which form the basis for $\hat{H}_{\zeta\boldsymbol{\kappa}}$,

Eq. (2.6), transform into each other on application of symmetry operators of c_{3v}. In the same basis, the symmetry operators acting on $\hat{H}_{\zeta\boldsymbol{\kappa}}$ take the form of matrices

$$\Gamma^{\zeta\boldsymbol{\kappa}}(\hat{c}_3) = \begin{pmatrix} 0 & 0 & -1 \\ -1 & 0 & 0 \\ 0 & 1 & 0 \end{pmatrix}, \qquad \Gamma^{\zeta\boldsymbol{\kappa}}(\hat{s}_x) = s\zeta \begin{pmatrix} 1 & 0 & 0 \\ 0 & 0 & 1 \\ 0 & 1 & 0 \end{pmatrix}. \tag{2.7}$$

For the inversion-symmetric superlattice perturbation, the singlet eigenstate of $\hat{H}_{\zeta\boldsymbol{\kappa}}$ is given by $\boldsymbol{v}_s = \frac{1}{\sqrt{3}}(1, -1, -1)$. The action of matrices from Eq. (2.7) on this state show that it transforms according to the one-dimensional irreducible representations of c_{3v}: either A_1 for $s\zeta = 1$ or A_2 for $s\zeta = -1$, indicating evenness or oddness under $\hat{s}_x$ respectively. Similarly, the doublet states of $\hat{H}_{\zeta\boldsymbol{\kappa}}$, $\boldsymbol{v}_+ = \frac{1}{\sqrt{3}}\left(\sqrt{2}, \frac{1}{\sqrt{2}}, \frac{1}{\sqrt{2}}\right)$ and $\boldsymbol{v}_- = \frac{1}{\sqrt{2}}(0, 1, -1)$ transform as the two-dimensional irreducible representation, E, and their degeneracy is therefore protected by the c_{3v} symmetry.

The three anisotropic sDPs can be understood using the compatibility relations in the group appropriate for the sBZ edge, $c_h = \{id, \hat{s}_x\}$. This group only supports one-dimensional irreducible representations A_1 and A_2 with the doublet states reducing as $E = A_1 + A_2$. For a given band, $s = \pm 1$, the split bands at $\boldsymbol{\kappa}$ and $-\boldsymbol{\kappa}$ belong to different irreducible representations of c_h and therefore cannot be joined along the sBZ edge. Instead, if both of these bands are closer to zero energy than the doublet states, they must each be joined to one of the doublet bands at the opposite sBZ corner. Thus, along the sBZ edge, a crossing of the split bands is required, resulting in the sDPs illustrated in the valence band for the top row of Fig. 2.2.

2.6 Microscopic Models

2.6.1 Point Charge Model

The point charge model analysed below mimics the effect of the quadrupole electric moment of the atoms in the top layer of the substrate. In application to the graphene-hBN system, we neglect the potentials of the quadrupole moments of the boron atom, which have only σ-orbitals occupied by electrons, and replace nitrogen sites by a point core charge $+2|e|$ compensated by the spread out cloud of the π-electrons, which we replace by a homogeneous background charge density, giving $-2|e|$ per hexagonal unit cell of the substrate. This model gives an example of an inversion-symmetric moiré superlattice. The matrix elements of the resulting perturbation, taken between sublattice Bloch states i and j ($i, j = A$ or B), acting on the low-energy Dirac spinors of the graphene K_+ valley, are given by the long wavelength components of

$$\delta H_{ij} = \frac{-2e^2}{4\pi\epsilon_0}\sum_{\boldsymbol{R}_N}\int dz \frac{L^2\Phi^*_{K_+i}(\boldsymbol{r},z)\Phi_{K_+j}(\boldsymbol{r},z)}{\sqrt{(\boldsymbol{r}-\boldsymbol{R}_N)^2+(z-d)^2}}$$
$$= \frac{-2e^2}{4\pi\epsilon_0 a/\sqrt{3}}\sum_{\boldsymbol{g},\boldsymbol{g}',\boldsymbol{g}_N} I_{|\boldsymbol{K}_++\boldsymbol{g}|,|\boldsymbol{K}_++\boldsymbol{g}'|,|\boldsymbol{g}_N|} e^{i(\boldsymbol{g}'-\boldsymbol{g}+\boldsymbol{g}_N)\cdot\boldsymbol{r}} e^{i(\boldsymbol{g}\cdot\boldsymbol{\tau}_i-\boldsymbol{g}'\cdot\boldsymbol{\tau}_j)}. \quad (2.8)$$

In Eq. (2.8) $\boldsymbol{R}_N$ are positions of nitrogen sites and L^2 is the total area of the graphene sheet; $\Phi_{K_+,i}(\boldsymbol{r},z)$ are Bloch wavefunctions of graphene π-electrons exactly at the K_+ point. Then the Fourier transform has been used to write δH_{ij} in terms of a sum over substrate reciprocal lattice vectors, $\boldsymbol{g}_N$, and graphene reciprocal lattice vectors, $\boldsymbol{g}$ and $\boldsymbol{g}'$. Nearest neighbour vectors, $\boldsymbol{\tau}_{i=A/B} = \pm(0, a/\sqrt{3})$ are the same as in Fig. 1.1. The homogeneous background charge has not been included in Eq. (2.8) since its only role is to exclude $\boldsymbol{g}_N = 0$ from the sum. The long wavelength terms in the first exponential of the second line of Eq. (2.8) determine $\boldsymbol{b}_m = -(\boldsymbol{g}'-\boldsymbol{g}+\boldsymbol{g}_N)$. The dimensionless integral,

$$I_{Q,Q',g_N} = \frac{32a_0^3}{27(a/\sqrt{3})^3}\int dq_z dq_z' \frac{\psi^*(Q,q_z)e^{i(q_z-q_z')\cdot d}\psi(Q',q_z')}{g_N^2+(q_z-q_z')^2},$$

is written in terms of the Fourier transform of the hydrogen-like graphene $\mathrm{P^z}(\boldsymbol{r},z)$ orbitals with an effective Bohr radius a_0,

$$\psi(Q,q_z) = \frac{\pi}{a_0^{3/2}}\frac{1}{2\pi}\int d\boldsymbol{r}dz e^{-i(\boldsymbol{Q}\cdot\boldsymbol{r}+q_z z)}\mathrm{P^z}(\boldsymbol{r},z)$$
$$= \frac{-64ia_0q_z}{(1+4a_0^2(Q^2+q_z^2))^3}.$$

The integral, I_{Q,Q',g_N}, rapidly decays as a function of the magnitude of all its arguments so that we limit the sum in Eq. (2.8) to only several terms such that $|\boldsymbol{K}_+ + \boldsymbol{g}| = |\boldsymbol{K}_+ + \boldsymbol{g}'| = |\boldsymbol{K}_+|$, with $I = I_{K_+,K_+,g_0}$ where $g_0 = \frac{4\pi}{\sqrt{3}a(1+\delta)}$.

The carbon $2p_z$ orbitals may have a different effective Bohr radius compared to hydrogen.The range of values quoted for $\tilde{v} = \frac{2e^2}{4\pi\epsilon_0(a/\sqrt{3})}I$ in Table 2.1 corresponds to the interval $0.27\,\text{Å} \le a_0 \le 0.53\,\text{Å}$, indicated by the black double-arrow in Fig. 2.4, where the interlayer separation $3.22\,\text{Å} \le d \le 3.5\,\text{Å}$ is taken from Ref. [24]. The resulting superlattice perturbation and dispersion surfaces are shown graphically in Fig. 2.5.

Both the dominance of the simplest moiré harmonics, and the finite values for the off-diagonal terms u_1 and u_2, stem from the three-dimensional treatment of the substrate potential. The potential is strongest near the substrate, and therefore a greater proportion of the integral I_{Q,Q',g_N} comes from the region near the substrate, where the graphene $2p_z$ orbitals are broad and therefore have both rapidly decaying Fourier components and significant overlap with their neighbours. This contrasts

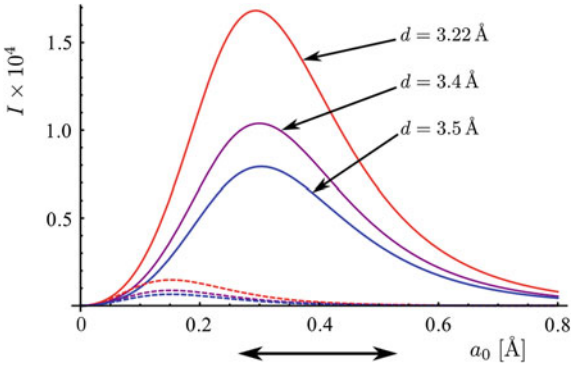

Fig. 2.4 *Solid lines* show the dimensionless integral I, as a function of the effective Bohr radius of the graphene $2p_z$ orbitals, for various choices of interlayer separation d. To demonstrate convergence of the sum in Eq. (2.8), *dashed lines* show I_{2K_+,K_+,g_0} for the same values of d

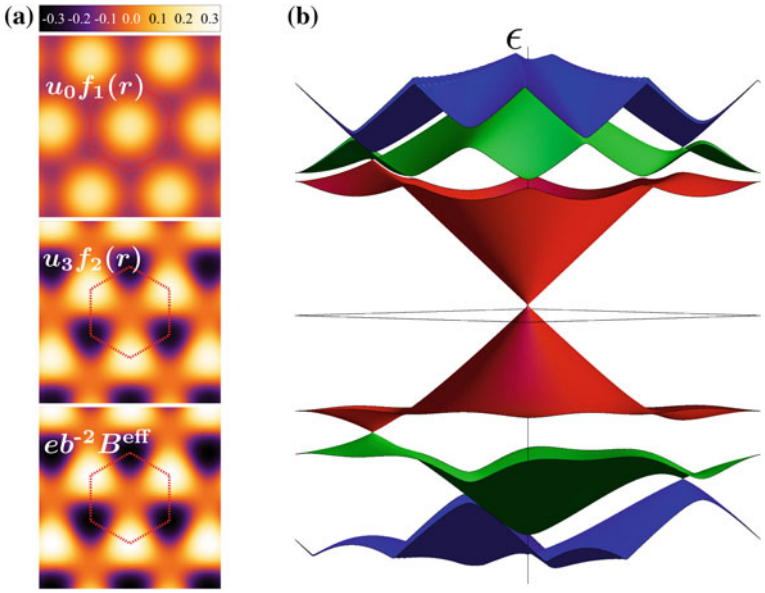

Fig. 2.5 **a** The simple potential modulation, $u_0 f_1(\boldsymbol{r})$, the local sublattice asymmetry, $u_3 f_2(\boldsymbol{r})$, and pseudo-magnetic field, $eb^{-2} B^{\text{eff}} = u_1 f_2(\boldsymbol{r})$ for the choice of parameters corresponding to the point charge model or the hopping model scaled so that $|u_0| + |u_1| + |u_3| = 0.15$. **b** The corresponding miniband spectra

with the model employed in Ref. [9] which is based on a two-dimensional substrate potential resulting in $u_1 = u_2 = 0$.

2.6.2 Graphene-hBN Hopping Model

In Ref. [10], Kindermann et al. modelled a hBN substrate as a lattice of $2p_z$ orbitals onto which the graphene electrons can hop. This treatment, extended from a model of twisted bilayer graphene [25], assumed equal values for the hopping integral to the boron and nitrogen sites, with the difference between the two sublattices arising from their different on-site energies. Here we consider an inversion-symmetric version of the hopping model of Ref. [10], assuming that coupling between graphene and the hBN layer is dominated by the hopping to only one of the two sublattices (e.g. boron). Using $\boldsymbol{k}\cdot\boldsymbol{p}$ theory (Sect. 1.4), this coupling can be written in the basis of graphene K_+ valley Bloch states, $(\Phi_{K_+,A}, \Phi_{K_+,B})$, as [10],

$$\begin{aligned}\delta\hat{H} &= \hat{H}_{\text{int}}\frac{1}{\epsilon - V - m}\hat{H}_{\text{int}}^{\dagger},\\ \hat{H}_{int} &= \frac{\gamma}{3}\sum_{n=0,1,2} e^{-i\left(\hat{R}_{\frac{2\pi n}{3}}\boldsymbol{\kappa}\right)\cdot\boldsymbol{r}}\begin{pmatrix} e^{i\frac{2\pi n}{3}} \\ e^{-i\frac{2\pi n}{3}}\end{pmatrix}.\end{aligned} \tag{2.9}$$

Neglecting a non-oscillatory term, which corresponds to a trivial constant energy shift, Eq. (2.9) as applied to graphene electrons in valley K_+, leads to the moiré Hamiltonian, Eq. (2.2), with

$$\{u_{i=0,\ldots 3}\} = \frac{\gamma^2/(vb)}{9(m+V)}\left\{\frac{1}{2}, \frac{-\delta}{\sqrt{\delta^2+\theta^2}}, \frac{\theta}{\sqrt{\delta^2+\theta^2}}, -\frac{\sqrt{3}}{2}\right\}.$$

The parameters of the superlattice perturbation given in Table 2.1 of the main text, correspond to $\gamma = 0.3\,\text{eV}$, $V = 0.8\,\text{eV}$ and $m = 2.3\,\text{eV}$, in accordance with Ref. [10]. For the perfectly aligned system, we always find $u_2 = 0$, which is a consequence of the reflection symmetries present in the perfectly aligned substrate-graphene system (see Sect. 2.5).

2.6.3 Inversion Asymmetric Microscopic Models

To generate the inversion-asymmetric perturbation terms in the microscopic models discussed above, we now account for both the nitrogen and the boron sublattice of the hBN underlay. This is achieved by taking the moiré perturbation,

$$\delta\hat{H}'(\boldsymbol{r}) = \delta\hat{H}(\boldsymbol{r}) + v_B\,\delta\hat{H}\left(\boldsymbol{r} - \frac{4\pi}{3b^2}\boldsymbol{b}_0\right). \tag{2.10}$$

Here $\delta\hat{H}(\boldsymbol{r})$ is the Hamiltonian (2.8), and $v_B \ll 1$ controls the strength of the perturbation due to the boron sites with respect to that of the nitrogen sites. The choice of origin used for $\delta\hat{H}'$ in Eq. (2.10) corresponds to the location in the moiré unit cell with the nitrogen site directly below the centre of the graphene hexagon; whereas the coordinate shift $-\frac{4\pi}{3b^2}\boldsymbol{b}_0$ in the last terms of Eq. (2.10) corresponds to the position with the boron site directly under the centre of the graphene hexagon. This coordinate change in the last term affects a rotation in the parameter space[3] for $v_B H(\boldsymbol{r} - \frac{4\pi}{3b^2}\boldsymbol{b}_0)$

$$\begin{pmatrix} v_B u_i \\ v_B \tilde{u}_i \end{pmatrix} \to \hat{R}_{\alpha 2\pi/3} \begin{pmatrix} v_B u_i \\ v_B \tilde{u}_i \end{pmatrix}, \quad \alpha = \begin{cases} -1 & \text{for } i = 0 \\ 1 & \text{otherwise} \end{cases}. \tag{2.11}$$

Hence the parameters are given by

$$\begin{aligned} \{u_{i=0,\ldots 3}\} &= v^+ \left\{ \frac{1}{2}, \frac{-\delta}{\sqrt{\delta^2+\theta^2}}, \frac{\theta}{\sqrt{\delta^2+\theta^2}}, -\frac{\sqrt{3}}{2} \right\}, \\ \{\tilde{u}_{i=0,\ldots 3}\} &= v^- \left\{ \frac{-1}{2}, \frac{-\delta}{\sqrt{\delta^2+\theta^2}}, \frac{\theta}{\sqrt{\delta^2+\theta^2}}, -\frac{\sqrt{3}}{2} \right\}, \end{aligned} \tag{2.12}$$

where $v^+ = \tilde{v}\left(1 - \frac{v_B}{2}\right)$ and $v^- = \tilde{v}\frac{\sqrt{3}v_B}{2}$. It is interesting to note that, for this choice of parameters, the zero-energy Dirac point remains un-gapped, due to cancellation of the two terms in Eq. (2.4) that is peculiar to this choice of parameters. However, gaps in the sDPs are opened as expected.

2.7 Conclusion

Using a general symmetry-based approach, we have provide a classification of generic miniband structures for electrons in graphene placed on substrates with the hexagonal Bravais symmetry. In particular, we identify conditions at which the first moiré miniband is separated from the rest of the spectrum by either one, or a group of three isolated mini Dirac points, and is not obscured by dispersion surfaces coming from other minibands. In such cases the Hall coefficient exhibits two distinct alternations of its sign as a function of charge carrier density. Other experimental consequences of the miniband spectra will be discussed in the next three chapters.

[3] In Eqs. (2.5) and (2.6) this transformation is equivalent to a gauge transform and therefore leaves the bandstructure unaltered.

References

1. C.R. Dean, A.F. Young, I. Meric, C. Lee, L. Wang, S. Sorgenfrei, K. Watanabe, T. Taniguchi, P. Kim, K.L. Shepard, J. Hone, Nat. Nano. **5**, 722 (2010)
2. J. Xue, J. Sanchez-Yamagishi, D. Bulmash, P. Jacquod, A. Deshpande, K. Watanabe, T. Taniguchi, P. Jarillo-Herrero, B.J. LeRoy, Nat. Mater. **10**, 282 (2011)
3. M.S. Bresnehan, M.J. Hollander, M. Wetherington, M. LaBella, K.A. Thurnbull, R. Cavalero, D.W. Snyder, J.A. Robinson, ACS Nano **6**, 5234 (2012)
4. R. Decker, Y. Wang, V.W. Brar, W. Regan, H.-Z. Tsai, Q. Wu, W. Gannett, A. Zettl, M.F. Crommie, Nano Lett. **11**, 2291 (2011)
5. A.S. Mayorov, R.V. Gorbachev, S.V. Morozov, L. Britnell, R. Jalil, L.A. Ponomarenko, P. Blake, K.S. Novoselov, K. Watanabe, T. Taniguchi, A.K. Geim, Nano Lett. **11**, 2396 (2011)
6. E. Kim, T. Yu, E.S. Song, B. Yu, Appl. Phys. Lett. **98**, 262103 (2011)
7. H. Wang, T. Taychatanapat, A. Hsu, K. Watanabe, T. Taniguchi, P. Jarillo-Herrero, T. Palacios, IEEE Electron Device Lett. **32**, 1209 (2011)
8. M. Yankowitz, J. Xue, D. Cormode, J.D. Sanchez-Yamagishi, K. Watanabe, T. Taniguchi, P. Jarillo-Herrero, P. Jacquod, B.J. LeRoy, Nat. Phys. **8**, 382 (2012)
9. C. Ortix, L. Yang, J. van den Brink, Phys. Rev. B **86**, 081405 (2012)
10. M. Kindermann, B. Uchoa, D.L. Miller, Phys. Rev. B **86**, 115415 (2012)
11. J.R. Wallbank, A.A. Patel, M. Mucha-Kruczynski, A.K. Geim, V.I. Fal'ko, Phys. Rev. B **87**, 245408 (2013)
12. C.-H. Park, L. Yang, Y.-W. Son, M.L. Cohen, S.G. Louie, Nat. Phys. **4**, 213 (2008)
13. J.M.B. Lopes dos Santos, N.M.R. Peres, A.H. Castro Neto, Phys. Rev. Lett. **99**, 256802 (2007)
14. R. Bistritzer, A.H. MacDonald, Phys. Rev. B **81**, 245412 (2010)
15. R. Bistritzer, A.H. MacDonald, Phys. Rev. B **84**, 035440 (2011)
16. J.M.B. Lopes dos Santos, N.M.R. Peres, A.H. Castro Neto, Phys. Rev. B **86**, 155449 (2012)
17. S.V. Iordanskii, A. Koshelev, JETP Lett. **41**, 574 (1985)
18. M.S. Foster, A.W.W. Ludwig, Phys. Rev. B **73**, 155104 (2006)
19. A.F. Morpurgo, F. Guinea, Phys. Rev. Lett. **97**, 196804 (2006)
20. J.C. Slonczewski, P.R. Weiss, Phys. Rev. **109**, 272 (1958)
21. C.-H. Park, L. Yang, Y.-W. Son, M.L. Cohen, S.G. Louie, Phys. Rev. Lett. **101**, 126804 (2008)
22. F. Guinea, T. Low, Phil. Trans. R. Soc. A **368**, 5391 (2010)
23. D.R. Hofstadter, Phys. Rev. B **14**, 2239 (1976)
24. G. Giovannetti, P.A. Khomyakov, G. Brocks, P.J. Kelly, J. van den Brink, Phys. Rev. B **76**, 073103 (2007)
25. M. Kindermann, P.N. First, Phys. Rev. B **83**, 045425 (2011)

Springer

http://www.springer.com/978-3-319-07721-5

Electronic Properties of Graphene Heterostructures with Hexagonal Crystals

Wallbank, J.

2014, XIII, 95 p. 38 illus., 22 illus. in color., Hardcover
ISBN: 978-3-319-07721-5